

## Research paper

## A novel PET model based volt/var control of AC–DC hybrid distribution network

Kun Yu<sup>a,\*</sup>, Bu Xue<sup>a</sup>, Fangyuan Gu<sup>a</sup>, Haochen Hua<sup>a</sup>, Yubo Yuan<sup>b</sup>, Qiang Li<sup>b</sup><sup>a</sup> College of Energy & Electrical Engineering, Hohai University, Nanjing, China<sup>b</sup> State Grid Jiangsu Electric Power CO., LTD., Research Institute, Nanjing, China

## ARTICLE INFO

## Article history:

Received 25 October 2021

Received in revised form 17 January 2022

Accepted 21 January 2022

Available online xxxx

## Keywords:

Power electronic transformer

Loss model

Power flow calculation

Volt/var control

Multi-objective optimization

## ABSTRACT

With the explosive growth of distributed renewable energy connected to the power system, the application of AC–DC hybrid distribution network with power electronic transformer (PET) becomes more and more extensive. An equivalent loss model is formulated from the perspective of the internal topology of PET. Then, a novel PET power flow model is established to obtain the relationship between the three ports. On this basis, reactive power of PV nodes connecting PET and distributed renewable generation is modified by establishing an equivalent impedance matrix, thus the forward–backward sweep load flow calculation method is improved for power flow calculation and volt/var control of distribution network. Different from traditional reactive optimization methods, a multi-objective reactive power optimization model considering the PET and two types of photovoltaic converters is established in this paper, with the targets of minimizing voltage deviation and power loss simultaneously. Finally, the numerical simulation shows the accuracy, rationality, and feasibility of the proposed method.

© 2022 Published by Elsevier Ltd. This is an open access article under the CC BY-NC-ND license (<http://creativecommons.org/licenses/by-nc-nd/4.0/>).

## 1. Introduction

With the globalized carbon neutrality target, more and more clean distributed generations (DGs) will be accommodated in the distribution network (DN) in the near future. The high penetration of large-scale DGs makes traditional DN change, and power electronic features in DN have become more and more obvious owing to the integration of power electronic converters and power electronic transformer (PET). As the interface of DGs, power electronic converters can promote the flexibility of AC–DC hybrid DN, but the problem brought by them cannot be ignored in the operation and control of DN (Huber and Kolar, 2019). PETs, including power electronic converters and high-frequency transformers, have been widely used in AC/DC hybrid DN due to their ability of controlling power flow and reactive power (Milczarek and Malinowski, 2020; Hua et al., 2022). The size and location of the converters can be optimized by designing the topology of PET, which makes AC–DC hybrid DN with high-permeability converters more compact (Das et al., 2021; Huang et al., 2020; She et al., 2013).

Taking into account both voltage quality and economic issues, the volt/var control problem of DN with DGs and PET is an interesting subject for further study. Photovoltaic inverters, capacitor

banks (CBs), and on-load tap changers (OLTCs) are used to optimize the reactive power of DN (Zhang and Xu, 2020; Ghofrani and Majidi, 2021; Tang et al., 2021). Photovoltaic inverters are used in Zhang and Xu (2020) for reactive power compensation, but they are not used in combination with PET, resulting in limited reactive power regulation capabilities. As traditional reactive power optimization methods, the regulation means of CBs and OLTCs are discrete with slow response, which has poor applicability of handling the frequent voltage violations (Ghofrani and Majidi, 2021; Tang et al., 2021). In addition to the regulation of the equipment, the optimization of the voltage regulation algorithm can also promote the economics of the power system operation (Hua et al., 2018). The volt/var control approaches are summarized in Table 1 with respect to various devices and types of DN. It is concluded that most of the volt/var control approaches are used through traditional devices such as OLTCs and CBs according to the review of recent 10 years of literature from Vijayan et al. (2021), Nazir et al. (2018), Xu et al. (2017), Howlader et al. (2018), Kraczy et al. (2017), Paul et al. (2021), Taghavi et al. (2012), Shah and Crow (2015), Ahmadi et al. (2014), Malekpour et al. (2012), Bottura and Borghetti (2014) and Salles et al. (2016). In the near future, more and more research will apply photovoltaic converters to realize volt/var control with the AC–DC hybrid DN. Moreover, it has a trend of combining the PET with photovoltaic converters to obtain optimized operation of the AC–DC hybrid DN. It is obvious that the volt/var control method that does not consider PET in the AC/DC hybrid DN is unsuitable. At present, considering

\* Corresponding author.

E-mail address: [kun.yu@vip.sina.com](mailto:kun.yu@vip.sina.com) (K. Yu).

## Nomenclature

PET	Power electronic transformer
DGs	Distributed generations
DN	Distribution network
CBs	Capacitor banks
OLTCs	On-load tap changers
DAB	Dual active bridge
NSGA-II	Non-dominated sorting genetic algorithm
CLCM	Constant loss coefficient method

the PET model accurately in DN and improving the power flow calculation including PET and DGs are the key technologies for reactive power optimization control.

Before studying the impact of PET on the reactive power control of DN, the first step is to formulate the power flow model of PET. Since PET contains many power electronic devices, the whole loss model is worthy of deep attention. The inside topology structure is the key factor to study the equivalent loss model of PET. The loss of PET mainly consists of switching devices and dual active bridge (DAB). From the perspective of the internal switching devices of the PET, a mathematical model of a virtual bridge arm is proposed and the power loss of modular multi-level converter has been calculated in [Christe and Dujic \(2017\)](#). However, universal modeling is required for different switching devices, and the structure of this model appears complicated. For the study of switching devices loss, the average power loss is calculated to reflect the effect of instantaneous temperature on the operation of IGBT, which provides a basis for the study of reducing IGBT power loss ([Bahman et al., 2018](#)). Though the Foster thermal model is established to reveal the relationship between IGBT loss and temperature rise, the causes of IGBT loss have not been further explored. The reduction of switching devices loss can be realized from the perspective of control strategies; see, e.g., [Liu et al. \(2017\)](#), [Flourentzou et al. \(2010\)](#). The loss model of switching devices is established in [Zhu et al. \(2020\)](#), [Baliga \(2013\)](#), [Wang et al. \(2017\)](#), [Bazzi et al. \(2012\)](#) and [Xu et al. \(2020\)](#), but the internal structure of PET and the application of the loss model in reactive power control are not considered. From the perspective of the DAB module inside PET, the function of DAB is to isolate different voltage levels and the internal high-frequency transformer of DAB is used to regulate the voltage. A new DAB module topology is proposed to solve the problem of the excessive number of power electronic switching devices in large-capacity PET ([Wang et al., 2021](#)). Nevertheless, only the power electronic devices in the DAB module are studied lacking the concern of core losses and winding losses. The loss model of the DAB module is established based on the special working state of the DAB module when the transformer is fully loaded. There is still a certain error regarding the actual transformation ratio, which may not be able to meet other operating conditions ([Hou and Li, 2020](#)). The aforementioned works summarize the research on the loss of switching devices and DAB separately. It is notable that the research about the loss model of multi-port PET combining with switching devices and DAB simultaneously has not been fully investigated, which makes the DN using multi-port PET exist certain errors in power flow calculation and reactive power optimization.

The application of PET makes the traditional power flow calculation method inapplicable ([Lu et al., 2019](#)), thus it is necessary to establish a power flow model of PET and improve the power flow algorithm. Since PET contains power electronic switching devices

which are different from ordinary transformers, it is important to obtain a power flow model considering conduction and switching power loss inside PET ([Sadigh et al., 2016](#)). In [Ju et al. \(2014\)](#), a method of solving the equivalent impedance matrix of PV nodes in forward–backward power flow calculation is proposed, which improves the processing capacity of PV nodes. However, the processing method in the DC system is not mentioned and is not combined with PET. A PET model considering the efficiency curves of PET obtained from laboratory measurements is developed in order to evaluate the impact of PET on distribution system performance ([Guerra and Martinez-Velasco, 2017](#)). Although the mathematical model of PET is analyzed, the impact of PET power loss on the system power flow is ignored, which may result in errors in the power flow calculation.

For the establishment of the volt/var model, a single-objective model is formulated in [Hua et al. \(2019\)](#). However, active power loss and voltage deviation cannot be coordinated sufficiently to acquire trade-off results. In [Syed et al. \(2018\)](#), it is necessary to judge whether the conditions are met each time before calling the model so that the calculation speed will be slow. A deep reinforcement learning approach is proposed to optimize energy management for the energy Internet ([Yeh et al., 2012](#)). However, the algorithm is not sufficiently suitable for a small-scale power system to solve a multi-objective model. The multi-objective optimization algorithm and its application in DN are introduced in [Ma et al. \(2021\)](#), [Parizad and Hatziaodoniu \(2020\)](#) and [Haddadian and Noroozian \(2019\)](#). A multi-objective model considering the PET model and two types of photovoltaic converters is proposed in this paper and a fast non-dominated sorting genetic algorithm (NSGA-II) is employed to solve the multi-objective model. Eventually, the reactive power compensation is reasonably allocated between the photovoltaic inverters and the PET by using the sensitivity coefficient adjustment method introduced in [Silva et al. \(2020\)](#). The major contribution of this paper is outlined as follows:

- From the perspective of power electronics, the internal loss composition of PET is firstly studied in this paper. Integrating switching device loss and DAB loss, a general expression of PET loss is derived. The conventional PET loss through repeated experiments to obtain measurement data in [Madhusoodhanan et al. \(2020\)](#) is avoided, which is conducive to the improvement and optimization of PET operation. In this sense, the loss of PET can be fully quantified and analyzed, and various measures can be taken to suppress the loss and optimize the performance of PET.
- The power flow between the three ports of PET makes the power flow model difficult to be established, therefore the PET power flow model is divided into two simplified models to obtain the power flow relationship between the three ports. In contrast to the method of ignoring the loss and considering the loss as a constant; see, e.g., [Liu et al. \(2018\)](#) and [Coppo et al. \(2017\)](#), the power flow model in this paper is more advantageous in the sense so that enough calculation accuracy can be guaranteed in the research of power flow optimization.
- The conventional reactive power regulation devices are no longer adequate due to their slow response speed and limited frequency of operation ([Ghofrani and Majidi, 2021](#); [Tang et al., 2021](#)), therefore the coordination between the reactive power of the PET port and the photovoltaic inverters is implemented in this paper. The sensitivity adjustment method is used to allocate the reactive power reasonably between PET and photovoltaic inverters, avoiding poor DN performance caused by unreasonable reactive power distribution, increasing the resilience of DN.

**Table 1**  
Summary of volt/var control approaches.

Year	Reference	Devices				DN	
		OLTCs	CBS	Converters	PET	AC	AC–DC
2017–2021	Vijayan et al. (2021), Nazir et al. (2018), Xu et al. (2017)	✓	✓	✓		✓	
	Howlader et al. (2018)			✓		✓	
	Kraiczky et al. (2017)	✓		✓		✓	
	Paul et al. (2021)		✓	✓			✓
2012–2016	Taghavi et al. (2012)	✓					✓
	Shah and Crow (2015)				✓	✓	✓
	Ahmadi et al. (2014), Malekpour et al. (2012)	✓	✓			✓	
	Bottura and Borghetti (2014)	✓				✓	
	Salles et al. (2016)		✓			✓	

- A multi-objective optimization model under the DN containing PET and photovoltaic converters is formulated in this paper. Since voltage deviation and power loss cannot be optimized at the same time, the NSGA-II algorithm is utilized to obtain a compromise between voltage deviation and power loss. The simulation results show that the voltage quality and active power loss of the DN have been significantly improved under the condition of making full use of PET and photovoltaic converters, thus optimizing the operation of the DN.

The rest of this paper is organized as follows: Section 2 establishes the equivalent power loss model of PET. In Section 3, the power flow calculation method for AC/DC hybrid DN with DGs is studied, in which the power loss of PET is considered. Based on the established loss model and improved power flow method, a reactive power optimization model is proposed in Section 4. Cases studies are implemented in Section 5. Finally, the conclusion is drawn in Section 6.

## 2. Equivalent power loss model of PET

This paper mainly studies PET with three ports in AC/DC hybrid system, and its power loss cannot be ignored in the power flow calculation of DN. Because of the large number of power electronic devices, the calculation of the actual power loss of PET is relatively complicated. In this paper, the relationship between the three-port PET power loss and the electrical parameters of the ports is studied, in order to simplify the power loss calculation in the power flow algorithm and establish the connection between different power systems.

### 2.1. Topology of PET

The half-bridge MMC PET which is shown in Fig. 1 has three ports, namely high-voltage AC port, low-voltage AC port, and low-voltage DC port. Its internal structure can be divided into three parts. The first part is the half-bridge MMC rectifier. The second part is DAB, including a high-frequency inverter, high-frequency transformer, and high-frequency rectifier. The last part is the inverter.

### 2.2. Actual power loss model

In the total power loss of PET, the power loss of the IGBT module accounts for more than half (Rohner et al., 2010). However, the power loss of high-frequency transformer in PET cannot be ignored and the detailed power loss model of PET will be analyzed.

#### 2.2.1. Power electronic devices

Based on the theoretical research in Rohner et al. (2010), the power loss of power electronic devices is mainly composed of IGBT power loss and FWD power loss. The power loss of both IGBT and FWD consists of three parts which are conduction loss, switching loss, and cut-off loss. While analyzing the power loss, the cut-off loss can always be ignored, because it is far less than the other two kinds of loss. The switching loss includes turn-on loss and turn-off loss, and the turn-on loss of FWD can also be ignored because it is far less than the turn-off loss of FWD (Sadigh et al., 2016).

The conduction losses of IGBT and FWD which are in the same module can be expressed as:

$$\begin{cases} P_{SS} = \frac{1}{T} \int_0^T v_{CE}(t) i_C(t) \tau(t) dt \\ P_{DC} = \frac{1}{T} \int_0^T v_F(t) i_F(t) [1 - \tau(t)] dt \end{cases} \quad (1)$$

where  $P_{SS}$  and  $P_{DC}$  are the conduction losses of IGBT and FWD, respectively;  $v_{CE}$  is the collector–emitter voltage of IGBT, and  $v_F$  is the forward voltage of FWD;  $i_C$  is the collector current of IGBT, and  $i_F$  is the forward current of FWD;  $\tau$  is the duty cycle, and  $T$  is the cycle of the modulation wave.

With the output characteristic curve of IGBT and FWD, the collector–emitter voltage of IGBT and the forward voltage of FWD can be shown as follows (Sadigh et al., 2016):

$$\begin{cases} v_{CE}(t) = V_{CE0} + r_{CE} i_C(t) \\ v_F(t) = V_{F0} + r_F i_F(t) \end{cases} \quad (2)$$

where  $V_{CE0}$  and  $V_{F0}$  are the threshold voltage of IGBT and FWD, respectively;  $r_{CE}$  and  $r_F$  are the equivalent resistance of IGBT and FWD, respectively.

The modulation scheme of the modular multilevel rectifier module is carrier phase-shifted modulation, and the modulation scheme of the inverter module is sinusoidal pulse width modulation. If the condition is given as follows:

$$i_C(t) = i_F(t) = I_s \sin(\omega t) \quad (3)$$

the conduction loss can be obtained as follows:

$$\begin{cases} P_{SS} = \left(\frac{1}{2\pi} + \frac{M}{8}\right) V_{CE0} I_s + \left(\frac{1}{8} + \frac{M}{3\pi}\right) r_{CE} I_s^2 \\ P_{DC} = \left(\frac{1}{2\pi} - \frac{M}{8}\right) V_{F0} I_s + \left(\frac{1}{8} - \frac{M}{3\pi}\right) r_F I_s^2 \end{cases} \quad (4)$$

where  $M$  is the modulation ratio of the modulation scheme (Sadigh et al., 2016).

The switching losses of IGBT and FWD which are in the same module can be shown as follows:

$$\begin{cases} P_{SW} = (E_{SW(on)} + E_{SW(off)}) n_{SW} \frac{I_s}{I_{SN}} \frac{U_s}{U_{SN}} \\ P_{Tr} = E_{Diode(off)} n_{SW} \frac{I_s}{I_{SN}} \frac{U_s}{U_{SN}} \end{cases} \quad (5)$$

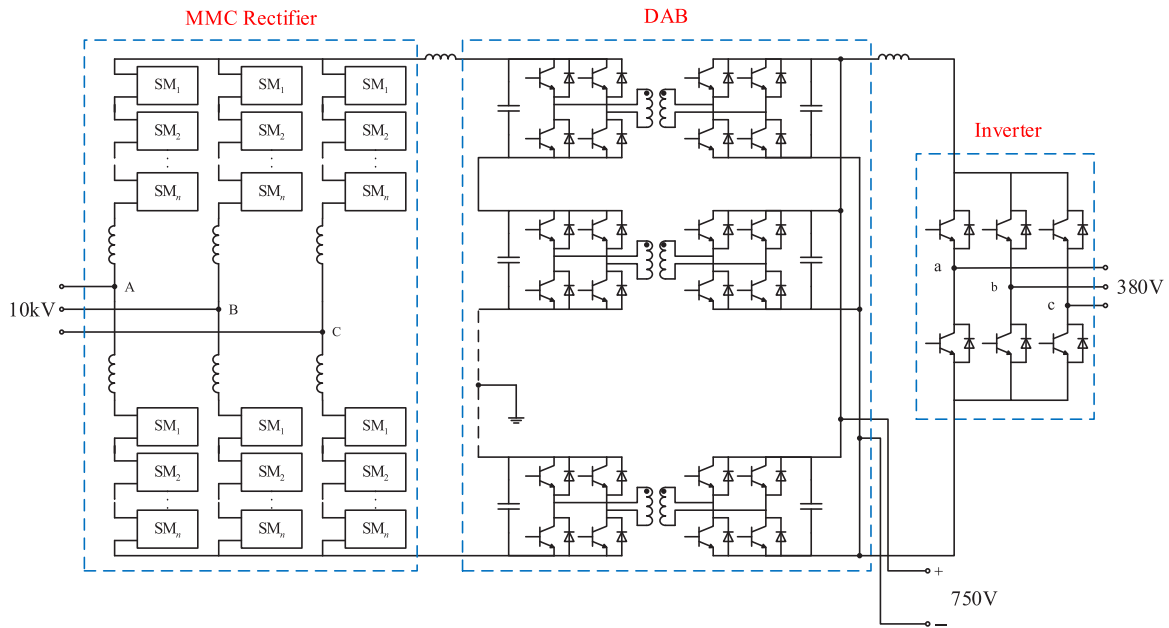


Fig. 1. Topology of PET.

where  $P_{SW}$  and  $P_{rr}$  are the switching losses of IGBT and FWD, respectively;  $E_{SW(on)}$  and  $E_{SW(off)}$  are the turn-on and turn-off energy loss per pulse of IGBT, respectively;  $E_{Diode(off)}$  is the turn-off energy loss per pulse of FWD;  $n_{SW}$  is the number of actions in a cycle;  $I_{sN}$  and  $U_{sN}$  are the rated current and voltage, respectively;  $I_s$  and  $U_s$  are the actual operating current and voltage, respectively.

The actual power loss of power electronic devices can be expressed as:

$$P_{loss} = n(P_{SS} + P_{DC} + P_{SW} + P_{rr}) \quad (6)$$

where  $P_{loss}$  is the actual power loss of power electronic devices;  $n$  is the number of IGBT modules.

As is shown in (4) and (5), in addition to the actual operating current and voltage, other variables are only related to the internal operation mode of PET. So the power loss of power electronic devices is only affected by the actual operating current of the port which is one of the external parameters of PET.

### 2.2.2. High-frequency transformer

A High-frequency transformer only exists in the DAB module. Based on the theoretical research in Roshen (2007), the power loss of the high-frequency transformer is mainly composed of core loss and winding loss. The core loss is a fixed value, which is only related to the material of the iron core in the transformer. The winding loss can be described as follows:

$$P_{Cu} = (R_{dc1} + R_{ac1}) \left( \frac{I_{s1}}{2} \right)^2 + (R_{dc2} + R_{ac2}) \left( \frac{I_{s2}}{2} \right)^2 \quad (7)$$

where  $P_{Cu}$  is the winding loss;  $I_{s1}$  and  $I_{s2}$  are the actual operating current of the high-voltage side and low-voltage side of the high-frequency transformer, respectively;  $R_{dc1}$  and  $R_{dc2}$  are the DC equivalent copper resistance of the high-voltage side and low-voltage side of the high-frequency transformer, respectively;  $R_{ac1}$  and  $R_{ac2}$  are the AC equivalent copper resistance of the high-voltage side and low-voltage side of the high-frequency transformer, respectively.

As is shown in (7), in addition to the actual operating current of the high-voltage side and low-voltage side of the high-frequency transformer, other variables are only related to the internal operation mode of PET. Therefore, the actual power loss of PET is affected by the actual operating current of the port and the fixed core loss.

### 2.3. Equivalent power loss model

Based on the relationship between the three ports of PET, the internal power loss of PET can be equivalent to the two modules, which are the power loss of the “high-voltage AC port to low-voltage AC port” module and the power loss of the “high-voltage AC port to low-voltage DC port” module.

Through the study of the actual power loss, the power loss of PET is only affected by the actual operating current, which is related to  $I^2$ ,  $I$  and constant. The equivalent power loss model can be described as follows:

$$\begin{cases} P_{loss-PET} = P_{loss-ac} + P_{loss-dc} \\ P_{loss-ac} = a_2 I_{ac}^2 + a_1 I_{ac} + a_0 \\ P_{loss-dc} = b_2 I_{dc}^2 + b_1 I_{dc} + b_0 \end{cases} \quad (8)$$

where  $P_{loss-PET}$ ,  $P_{loss-ac}$ , and  $P_{loss-dc}$  represent the power loss of PET, “high-voltage AC port to low-voltage AC port” module and “high-voltage AC port to low-voltage DC port” module, respectively;  $a_2$ ,  $a_1$ , and  $a_0$  are the coefficients of the AC port;  $b_2$ ,  $b_1$ , and  $b_0$  are the coefficients of the DC port.  $I_{ac}$  and  $I_{dc}$  are the current of low-voltage AC port and low-voltage DC port, respectively.

The general power loss formula of the two modules can be expressed as:

$$P = k_2 I^2 + k_1 I + k_0 \quad (9)$$

where  $k_2$ ,  $k_1$  and  $k_0$  are all larger than 0, which are not affected by external working conditions of PET.

According to Fig. 1, the module “high-voltage AC port to low-voltage AC port” is composed of the MMC rectifier, DAB, and inverter. Nevertheless, the inverter is not included in the “high-voltage AC port to low-voltage DC port” module. On the basis of (4), (5), and (7), the coefficients in (8) are analyzed as follows:

$a_2$  is related to the conduction loss of the MMC rectifier and inverter, and the winding loss of DAB;  $a_1$  is related to the conduction loss and switching loss of the MMC rectifier and inverter;  $b_2$  is related to the conduction loss of the MMC rectifier and the winding loss of DAB;  $b_1$  is related to the conduction loss and switching loss of the MMC rectifier; Both  $a_0$  and  $b_0$  are related to the core loss of DAB.

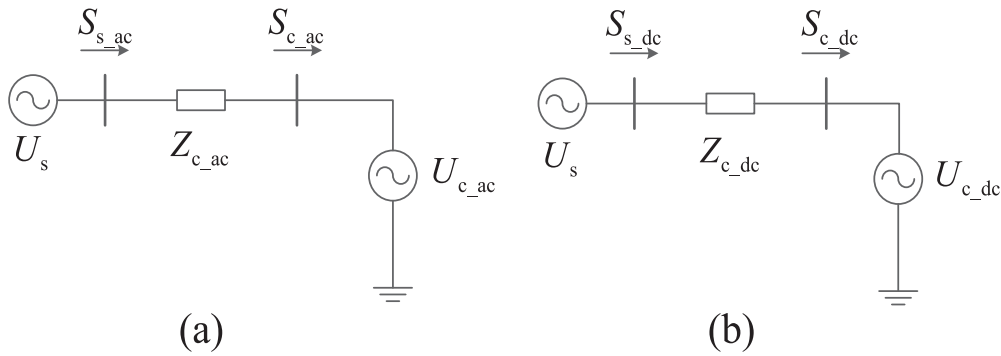


Fig. 2. Power flow model of PET: (a) “high-voltage AC port to low-voltage AC port” module; (b) “high-voltage AC port to low-voltage DC port” module.

### 3. Power flow calculation algorithm

The forward–backward sweep method is a practical power flow calculation method for DN, which can be divided into two stages. At the first stage, the power loss of each branch is calculated to obtain the power of the first node in the system, by using the known voltage of each node. At the second stage, each loss of voltage in the branch is calculated to obtain the voltage of each node, by using the voltage of the first node and the power of each node obtained at the first stage. However, the main drawback of this method is to calculate the voltage of PV nodes. If it is applied to AC/DC hybrid DN with high permeability for DGs, it will need to be improved. Also, if the DN contains the PET analyzed in Section 2, this method will need to be updated.

#### 3.1. Power flow model of PET

In Section 2, the three-port PET has been divided into two modules in this paper. The models of these two modules in power flow calculation are shown in Fig. 2.

In Fig. 2,  $U_s$  is the voltage of high-voltage AC port;  $Z_c$  is the equivalent impedance between the high-voltage port and the low-voltage port;  $U_c$  is the voltage which is controlled by the low-voltage port;  $S_c$  is the power controlled by the low-voltage port. The process of control is shown in (10) and (11). The power flow models of PET are formulated as:

$$\begin{cases} U_{c\_ac} = k_{ac}U_{ac} \\ P_{c\_ac} = P_{ac} + P_{ac\_loss} \\ P_{ac\_loss} = a_2I_{ac}^2 + a_1I_{ac} + a_0 \\ I_{ac} = \sqrt{\frac{P_{ac}^2 + Q_{ac}^2}{U_{ac}^2}} \end{cases} \quad (10)$$

$$\begin{cases} U_{c\_dc} = k_{dc}U_{dc} \\ P_{c\_dc} = P_{dc} + P_{dc\_loss} \\ P_{dc\_loss} = b_2I_{dc}^2 + b_1I_{dc} + b_0 \\ I_{dc} = \frac{P_{dc}}{U_{dc}} \end{cases} \quad (11)$$

where  $U_{ac}$  and  $U_{dc}$  are the voltage of low-voltage AC port and low-voltage DC port, respectively;  $P_{ac}$  and  $P_{dc}$  are the active power of low-voltage AC port and low-voltage DC port, respectively;  $Q_{ac}$  is the reactive power of low-voltage AC port; Other parameters are as shown in (8). The PET power flow model is divided into two simplified models as expressed in (10) and (11), therefore the power flow relationship between the three ports is obtained.

#### 3.2. Correction of reactive power on PV nodes

While DGs work in an AC system, the nodes of DGs are PV nodes or PQ nodes. The ports of PET in the AC system are PV nodes because of the capability of reactive power compensation. The forward–backward sweep power flow method has a drawback of calculating the voltage of PV nodes. The voltage amplitude of PV nodes is related to the reactive power, but the PV nodes have fixed voltage amplitude, which will result in the error of reactive power in the calculation. In this paper, the reactive power of PV nodes at two different positions is modified by establishing the equivalent reactance matrix.

##### 3.2.1. PV nodes at the end of the system

The equivalent impedance matrix of PV nodes is defined as  $Z = R + jX$ , where  $R$  is the resistance matrix and  $X$  is the reactance matrix. The deviation of the current is expressed as  $\Delta I = \Delta\alpha + j\Delta\beta$ , where  $\alpha$  is the real part of the current and  $\beta$  is the imaginary part of the current. The deviation of the voltage is written as  $\Delta V = \Delta\lambda + j\Delta\gamma$ , where  $\lambda$  is the real part of the voltage and  $\gamma$  is the imaginary part of the voltage.

The relationship between the current and the voltage is  $\Delta V = Z\Delta I$ , then the deviation of the voltage is shown as follows:

$$\begin{cases} \Delta\lambda = R\Delta\alpha - X\Delta\beta \\ \Delta\gamma = X\Delta\alpha + R\Delta\beta \end{cases} \quad (12)$$

according to the fixed voltage amplitude of PV nodes, (12) can be further simplified (Ju et al., 2014). Then the deviation of the current is expressed as follows:

$$\begin{cases} \Delta\alpha = R\Delta\lambda|Z|^{-2} \\ \Delta\beta = -X\Delta\lambda|Z|^{-2} \end{cases} \quad (13)$$

After further derivation, the correction of reactive power is expressed as follows:

$$\Delta Q = -X^{-1}\Delta\lambda \quad (14)$$

In order to correct the reactive power of PV nodes, the equivalent reactance matrix must be established. The method is shown as follows:

$$|U_{pv}|^2 = (R + jX)\tilde{S}_{pv}^* \quad (15)$$

where  $\tilde{S}_{pv}^*$  is the conjugate complex power of the PV nodes.

According to (15), the calculating voltage of PV node  $i$  can be written as follows:

$$|U_{pvi}|^2 = \sum_{k=1}^n (R_{ik} + jX_{ik})\tilde{S}_{pvk}^* \quad (16)$$

where  $k$  is the number of PV nodes.

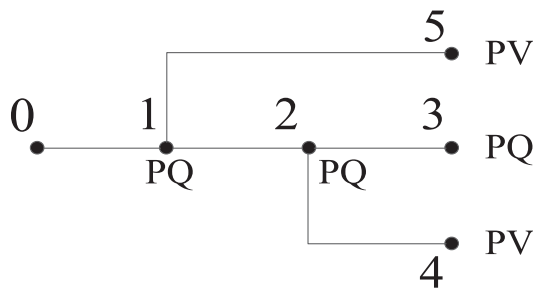


Fig. 3. Power System with two PV nodes.

If the conjugate complex power of PV nodes is shown in (17), the result can be shown in (18) combining with (16).

$$\begin{cases} \tilde{S}_{pvj}^* = j1 \\ \tilde{S}_{pvk}^* = 0 \quad k = 1, 2, \dots, n, k \neq j \end{cases} \quad (17)$$

$$X_{ij} = |U_{pvi}|^2 \quad (18)$$

where  $X_{ij}$  represents the element in the equivalent reactance matrix;  $i$  is the number of the row and  $j$  is the number of the column in the equivalent reactance matrix.

The example shown in Fig. 3 can be used to explain the specific method of establishing the equivalent reactance matrix.

As is shown in Fig. 3, the system has two PV nodes, the node No. 0 is balancing node, and the rest of nodes are PQ nodes. The equivalent reactance matrix is formulated as follows:

$$X = \begin{bmatrix} X_{11} & X_{12} \\ X_{21} & X_{22} \end{bmatrix} \quad (19)$$

where  $X$  is the equivalent reactance matrix.

If  $\tilde{S}_{pv4}^*$  is 0 and  $\tilde{S}_{pv5}^*$  is  $j1$ ,  $|U_{pv4}|$  and  $|U_{pv5}|$  are  $|U'_4|$  and  $|U'_5|$  by using the forward-backward sweep method for one time. Also, if  $\tilde{S}_{pv4}^*$  is  $j1$  and  $\tilde{S}_{pv5}^*$  is 0,  $|U_{pv4}|$  and  $|U_{pv5}|$  are  $|U''_4|$  and  $|U''_5|$  by using the same method. The result of  $X$  is presented as follows:

$$X = \begin{bmatrix} |U'_5|^2 & |U''_5|^2 \\ |U'_4|^2 & |U''_4|^2 \end{bmatrix} \quad (20)$$

### 3.2.2. PV nodes in the middle of the system

PV nodes in the middle of the system can be converted to the nodes at the end of the system by introducing virtual nodes (Ju et al., 2014). The example shown in Fig. 4 explains this conversion method.

In Fig. 4, the PV node No. 2 in the middle of the system can be converted to the PV node at the end of the system. Node No. 2 on the right is a PQ node and its power is 0. Then, the converted system can be handled using the same method mentioned above with PV nodes at the end of the system.

### 3.3. Procedure of the improved power flow calculation

As is shown in Fig. 5, the procedure of the improved power flow calculation based on PET loss model is shown as follows:

- (1) Establish the node admittance matrix and set the voltage of every node. The power of every node is the actual power.
- (2) Calculate the equivalent reactance matrix of PV nodes.
- (3) Calculate the nodes power of two low-voltage systems.
- (4) Calculate the node power of high-voltage port of PET by (10) and (11).
- (5) Calculate the nodes power of the high-voltage system.

- (6) Calculate the nodes voltage of the high-voltage system by using the nodes power calculated in Step 5.
- (7) Calculate the nodes voltage of two low-voltage ports of PET by (10) and (11).
- (8) Calculate the nodes voltage of two low-voltage systems by using the nodes power calculated in Step 3.
- (9) Determine whether all PV nodes meet the voltage convergence criterion which is shown as follows:

$$\max \left| |U_{pvi}^{(k)}| - U_{schi} \right| < \epsilon_{pv} \quad (21)$$

where  $\epsilon_{pv}$  is the convergence precision of PV nodes. If the node voltage meets the convergence criterion, go to Step 10. If else, go to Step 11.

- (10) Determine whether other nodes meet the convergence criterion which is shown as follows:

$$\max \left| U_i^{(k)} - U_i^{(k-1)} \right| < \epsilon \quad (22)$$

where  $\epsilon$  is the convergence precision of other nodes. If the node voltage meets the convergence criterion, go to Step 12. If else, go to Step 3.

- (11) Correct the reactive power of PV nodes by (14), the PV nodes voltage is replaced by the nodes voltage obtained by this calculation, then return to Step 3.
- (12) Finish the calculation and output the result.

## 4. Reactive power optimization model

For a three-port PET, its own port has the ability to control reactive power, which will also optimize the reactive power distribution in the system. The reactive power compensation capacity of the PET port has a certain adjustment range. Within its adjustment range, it can ensure that the system nodes containing DGs are within a reasonable voltage level range, and the active power loss in the system can be minimized through reactive power optimization. Based on the aforementioned power loss model of PET and improved power flow calculation method, this section will study the reactive power flow optimization of the AC-DC hybrid DN containing PET and photovoltaic converters.

### 4.1. Construction of reactive power optimization model

The reactive power optimization model of the DN is mainly established based on whether the system node voltage meets the reasonable operating range, and at the same time, the minimum active power loss must be guaranteed. The multi-objective function is expressed as follows:

$$f_1 = \min P_{Loss} \quad (23)$$

$$f_2 = \min \sum_{i=1}^n |V_i - V_N| \quad (24)$$

where  $P_{Loss}$  represents the total active power loss including DN, PET and photovoltaic converters;  $V_i$  represents the actual voltage value of node  $i$ ;  $V_N$  represents the rated voltage. The constraints of the above objective function are accounted for in the following including equality constraints and inequality constraints.

#### 4.1.1. Equality constraints

The two AC port nodes of PET are set as the PV nodes, and the DC port node of PET is set as the constant  $V$  node. The voltage of each port is set to the rated voltage, which is expressed as follows:

$$\begin{cases} V_{PET.HAC} = V_{N.HAC} \\ V_{PET.LAC} = V_{N.LAC} \\ V_{PET.DC} = V_{N.DC} \end{cases} \quad (25)$$

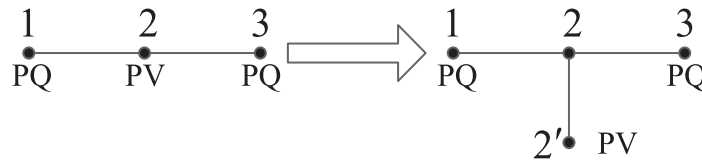


Fig. 4. Conversion method by introducing virtual nodes.

where  $V_{PET,HAC}$ ,  $V_{PET,LAC}$  and  $V_{PET,DC}$  are the port voltage amplitudes of the high-voltage AC side, low-voltage AC side and low-voltage DC side of PET, respectively;  $V_{N,HAC}$ ,  $V_{N,LAC}$  and  $V_{N,DC}$  represent the rated voltage amplitude of the high-voltage AC system, the low-voltage AC system and the low-voltage DC system, respectively.

Considering the power loss model of PET, the power balance constraint of the three-port PET is as follows:

$$P_{PET,HAC} = P_{PET,LAC} + P_{PET,DC} + P_{PET,loss} \quad (26)$$

where  $P_{PET,HAC}$ ,  $P_{PET,LAC}$  and  $P_{PET,DC}$  represent the port active power of the high-voltage AC system, the low-voltage AC system and the low-voltage DC system of PET, respectively.

#### 4.1.2. Inequality constraints

Since the DC port of three-port PET cannot control the reactive output, the three-port PET is equivalent to the two-port PET to simplify the reactive control structure of PET. The PET can be equivalent to two voltage source converters, and the modulation coefficient and modulation phase angle can be decoupled to control reactive power and port voltage, respectively. The inequality constraints of modulation coefficient and modulation phase angle are as follows:

$$\begin{cases} 0 \leq M_1, M_2 \leq 1 \\ -45^\circ \leq \delta_1, \delta_2 \leq 45^\circ \end{cases} \quad (27)$$

where  $M_1$  and  $M_2$  are the modulation coefficients of the primary and secondary sides, respectively;  $\delta_1$  and  $\delta_2$  are the modulation phase angles of the primary and secondary sides, respectively.

The allowable capacity constraints of PET ports are as follows:

$$\begin{cases} \sqrt{P_{PET,HAC}^2 + Q_{PET,HAC}^2} \leq S_{N,PET,HAC} \\ \sqrt{P_{PET,LAC}^2 + Q_{PET,LAC}^2} \leq S_{N,PET,LAC} \\ P_{PET,DC} \leq P_{N,PET,DC} \end{cases} \quad (28)$$

where  $S_{N,PET,HAC}$  and  $S_{N,PET,LAC}$  are the rated capacity of the high-voltage AC port and the low-voltage AC port of PET, respectively;  $P_{N,PET,DC}$  is the rated active capacity of the low-voltage DC port.

The constraints on the reactive power compensation capacity of the AC port of PET are as follows:

$$\begin{cases} 0 \leq Q_{PET,HAC,G} \leq Q_{PET,HAC,Gmax} \\ 0 \leq Q_{PET,LAC,G} \leq Q_{PET,LAC,Gmax} \end{cases} \quad (29)$$

where  $Q_{PET,HAC,G}$  and  $Q_{PET,LAC,G}$  represent the reactive power compensation capacity of the high-voltage side and low-voltage side of the AC port of PET, respectively;  $Q_{PET,HAC,Gmax}$  and  $Q_{PET,LAC,Gmax}$  represent the upper limit of the compensation capacity of the high-voltage side and the low-voltage side, respectively.

The output constraints of DGs are as follows:

$$\begin{cases} 0 \leq P_{DG,G} \leq P_{DG,Gmax} \\ 0 \leq Q_{DG,G} \leq Q_{DG,Gmax} \end{cases} \quad (30)$$

where  $P_{DG,G}$  and  $Q_{DG,G}$  represent the active output and reactive output of DGs, respectively;  $P_{DG,Gmax}$  and  $Q_{DG,Gmax}$  represent the upper limit of the active output and reactive output, respectively.

#### 4.2. Control models of PV converters

By controlling the active and reactive power output of the PV converter, the node voltage can be controlled within the rated operating range, and the maximum generation of photovoltaic power can be ensured, reducing other reactive power optimization investments. Photovoltaic can be directly connected to the DC grid, avoiding the link of the inverter, and can also be connected to the AC grid (Morshed and Fekih, 2020). Two control models of photovoltaic converters are analyzed in this paper. Photovoltaic is connected to the DC port of PET, eliminating the loss of the inverter. Since reactive power cannot be transmitted in the DC link, the PV converter runs at the unity power factor. Therefore, the control model of the PV converter connected to the DC port of PET is:

$$u^{dc}(t) = [P_{dc}(t), Q_{dc}(t)] = [P_{dc}(t), 0] \quad (31)$$

$$P_{loss}^{dc}(t) = (1 - \eta^{dc})S_N^{dc} \quad (32)$$

$$\eta^{dc}(t) = a_1 \exp(a_2 \frac{P_{dc}}{S_N^{dc}}) + b_1 \exp(b_2 \frac{P_{dc}}{S_N^{dc}}) \quad (33)$$

$$\xi = [a_1, a_2, b_1, b_2] \quad (34)$$

where  $u^{dc}(t)$  is the control variables of the PV converter;  $P_{dc}(t)$  and  $Q_{dc}(t)$  are the active power and reactive power of the PV converter, respectively;  $P_{loss}^{dc}(t)$  is the power loss of the PV converter;  $\eta^{dc}(t)$  is the operating efficiency function of the PV converter;  $S_N^{dc}$  is the capacity of PV converter;  $\xi$  is the control parameters of the operating efficiency function.

The control model of the PV inverter connected to the AC grid is:

$$u^{ac}(t) = [P^{ac}(t), Q^{ac}(t)] \quad (35)$$

where  $u^{ac}(t)$  is the control variable of the PV inverter;  $P^{ac}(t)$  and  $Q^{ac}(t)$  are the active and reactive power of the PV inverter, respectively. The loss model of PV inverter connected to AC grid is similar with PV converter connected to DC port of PET as shown in (33).

#### 4.3. Distribution of reactive power compensation

When the DN requires reactive power compensation, the reactive power compensation is shared by reactive power compensation devices according to their own sensitivity coefficient (Silva et al., 2020). The reactive power compensation in this paper is implemented between the PET and the PV inverters, and the sensitivity coefficients at these nodes need to be obtained. In the process of power flow calculation, the modified matrix equation is as follows:

$$\begin{bmatrix} \Delta P \\ \Delta Q \end{bmatrix} = \begin{bmatrix} \frac{\partial P}{\partial \theta} & \frac{\partial P}{\partial U} \\ \frac{\partial Q}{\partial \theta} & \frac{\partial Q}{\partial U} \end{bmatrix} \begin{bmatrix} \Delta \theta \\ \Delta U \end{bmatrix} \quad (36)$$

The above matrix equation is transformed as follows:

$$\begin{bmatrix} \Delta \theta \\ \Delta U \end{bmatrix} = \begin{bmatrix} S_{P\theta} & S_{Q\theta} \\ S_{PU} & S_{QU} \end{bmatrix} \begin{bmatrix} \Delta P \\ \Delta Q \end{bmatrix} \quad (37)$$

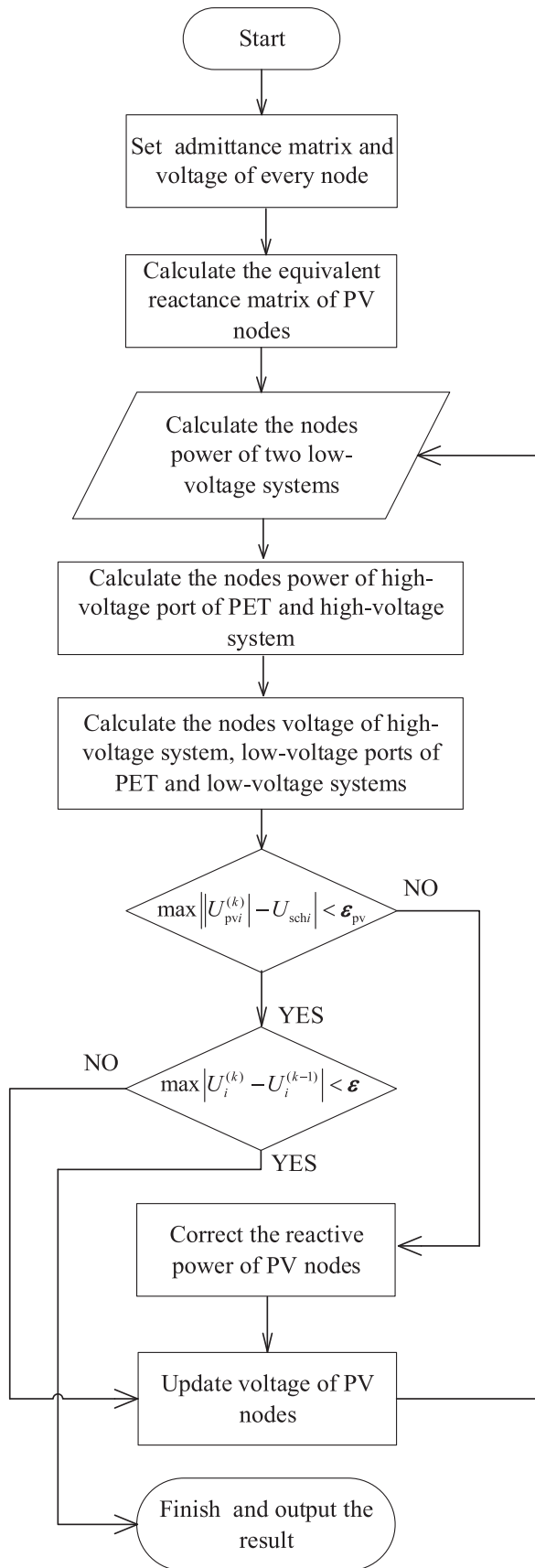


Fig. 5. Flow chart for the power flow calculation.

Table 2  
The parameters of switching devices.

Devices	Parameters	Value	Devices	Parameters	Value
IGBT	$V_{CE0}$	7/6 V	FWD	$V_{F0}$	8/7 V
	$r_{CE}$	1/540 $\Omega$		$r_F$	1/700 $\Omega$
	$E_{SW(on)}$	105 mJ		$E_{Diode(off)}$	60 mJ
	$E_{SW(off)}$	98 mJ		$U_{sN}$	900 V
	$U_{sN}$	900 V		$I_{sN}$	450 A
	$I_{sN}$	450 A			

The node voltage change caused by active and reactive power changes is as follows:

$$\Delta U_i = S_{PUj} \Delta P_j + S_{QUj} \Delta Q_j \quad (38)$$

where  $\Delta U_i$  is the voltage change of the node  $i$ ;  $\Delta P_j$  and  $\Delta Q_j$  are the active and reactive changes of node  $j$ , respectively;  $S_{PUj}$  is the active voltage sensitivity matrix and represents the impact of  $\Delta P_j$  on  $\Delta U_i$ , which can be ignored here;  $S_{QUj}$  is the reactive voltage sensitivity matrix.

Assuming that the voltage  $V_i$  of node  $i$  exceeds the limit, and  $V_N$  is the node voltage safety constraint, the voltage deviation is:

$$\Delta V_i = V_i - V_N \quad (39)$$

Then, the total reactive power compensation  $\Delta Q_i$  required by node  $i$  is:

$$\Delta Q_i = \frac{\Delta V_i}{S_{QUi}} \quad (40)$$

The PET and PV inverters reasonably distribute the reactive power compensation through the following formula, and the reactive power compensation distributed at node  $j$  is:

$$\Delta Q_j = \Delta Q_i \cdot \frac{S_{QU}(i, j)}{\sum_{j=1}^n S_{QU}(i, j)} \quad (41)$$

where  $S_{QU}(i, j)$  is the sensitivity coefficient of the voltage deviation, which represents the impact the reactive power injected into node  $i$  have on node  $j$ .

## 5. Case studies

### 5.1. Verification of PET equivalent power loss model

#### 5.1.1. Parameters

The parameters of switching devices of three-port PET are shown in Table 2, and the other devices are shown in Table 3.

#### 5.1.2. Simulation results

According to the parameters in Table 2 and Table 3, the parameters of equivalent power loss model in (8) are shown in Table 4.

The test operation efficiency of PET in each condition is shown in Table 5. The efficiency calculated by (8) and the parameters in Table 4 under the same conditions are also shown in Table 5 as the comparison. The error between the calculated result of the equivalent model and the actual test result satisfies the accuracy, so the equivalent power loss model is reasonable.

The constant loss coefficient method (CLCM) in Table 6 refers to the method of calculating PET loss based on 10% of the actual capacity of the PET port. As shown in Table 6, this paper studies the power loss and voltage deviation of DN under the conditions of light load (50%), normal load (100%), and heavy load (150%), respectively. Under the light, normal, and heavy load levels, the errors of power loss between CLCM and the proposed method are 44.84%, 14.95%, and 4.97%, respectively. It can be seen from

**Table 3**  
The parameters of other devices.

Parameters	Value	Parameters	Value
Capacity of PET	3MVA	$R_{dc1}$	0.00165 $\Omega$
Number of SMs in each bridge-arm	20	$R_{dc2}$	0.0035 $\Omega$
Voltage of one SM	1000 V	Core loss of high-frequency transformer	22.7 W
Voltage of high-voltage AC port	10 kV	Frequency of high-frequency transformer	1 kHz
Frequency of AC voltage	50 Hz	Ratio of high-frequency transformer	4:3
Number of DAB modules	10	Voltage of Low-voltage DC port	$\pm 750$ V
$R_{ac1}$	0.00159 $\Omega$	Voltage of Low-voltage AC port	380 V
$R_{ac2}$	0.00336 $\Omega$		

**Table 4**  
The parameters of equivalent power loss model.

Parameters	Value	Parameters	Value
$a_2$	0.074	$b_2$	0.073
$a_1$	32.054	$b_1$	31.267
$a_0$	113.5	$b_0$	113.5

**Table 5**  
The comparison of efficiency.

Current of low-voltage ports		Efficiency	
AC port	DC port	Test	Calculation
450 A	$\pm 450$ A	97.11%	98.05%
500 A	$\pm 500$ A	97.04%	97.71%
550 A	$\pm 550$ A	96.95%	97.34%
600 A	$\pm 600$ A	96.44%	96.96%
650 A	$\pm 650$ A	96.01%	96.55%
700 A	$\pm 700$ A	95.78%	96.11%

Table 6 that the method proposed in this paper is very different from CLCM under normal and light load levels. This is because the line loss is small due to the low load level, but the loss of PET is large as the comparison. At this time, if the loss of PET is ignored or CLCM is used to calculate the loss, it will have a negative impact on the operation and planning of DN. In the case of heavy load level, the line loss increases due to the increase in line current, which can reduce the negative impact of CLCM, but the proposed method in this paper cannot tolerate this calculation error. Under the light, normal, and heavy load levels, the errors of voltage deviation between CLCM and the proposed method are 9.58%, 0.81%, and 0.25%, respectively. At this moment, the volt/var optimization is not performed to achieve the optimal power flow, and the voltage deviation does not compromise with the power loss of DN, so the effect of CLCM on the voltage deviation error is not obvious. Therefore, this paper can more accurately consider the overall power loss and voltage deviation of DN, and provide a guarantee for the economic benefits and stable operation of DN.

## 5.2. Improved power flow calculation

### 5.2.1. Simulation parameters

In order to verify the feasibility of the power flow calculation method, the power flow of the IEEE 33-bus system is calculated. The adjusted structure of the system with new nodes in the DC system is shown in Fig. 6.

As is shown in Fig. 6, the blue nodes are the nodes in the AC system whose voltage is 380 V, the red nodes are the nodes in the DC system whose voltage is  $\pm 750$  V and the black nodes are the nodes in the AC system whose voltage is 10 kV. Node No. 28 is the high-voltage AC port of PET, node No. 29 is the low-voltage AC port of PET, and node No. 34 is the low-voltage DC port of PET. The voltage and power of nodes No. 29 and No. 29' can be controlled by (10). The voltage and power of nodes No. 34 and No. 34' can be controlled by (11). Besides the change of parameters in some nodes shown in Table 7, the rest parameters of the system are the same as those in Sun et al. (2021). The parameters of DGs nodes in the system are shown in Table 8.

### 5.2.2. Results

The node voltages of the power system, including the conditions within DGs and without DGs, are shown in Fig. 7 and Fig. 8. According to the results shown above, the voltage of the low-voltage system meets the appropriate operating range, and the voltage quality of the high-voltage system has been improved significantly due to the compensation of the DGs. The voltages of PV nodes are the same as the preset voltages, which demonstrates the effectiveness of the calculation method. Therefore, the improved forward-backward sweep power flow method based on PET is suitable for AC/DC hybrid DN with high penetration of DGs.

As shown in Table 9, the power flow calculation under different load conditions can achieve rapid convergence in a few iterations, and the calculation time is less than 40 ms, which has a faster calculation speed. At the same time, the convergence error is in the order of  $10^{-14}$ , which strongly guarantees the calculation accuracy. Due to the fast convergence characteristics of the improved power flow calculation, it saves time for the subsequent reactive power optimization program that contains thousands of power flow calculations and can realize fast reactive power optimization control.

### 5.3. Solution of reactive power optimization model

The NSGA-II algorithm is used to solve the reactive power optimization problem. The active power loss and node voltage deviation will be calculated by the aforementioned power flow calculation method. The variables in the NSGA-II are the reactive power compensation of the PET port and the output power of the photovoltaic converters in DN. The number of iterations is set to 700 and the population size is set to 100, then the problem is solved in the above-mentioned improved IEEE 33-bus system.

The node voltages of the 10 kV DN under the initial randomly generated 100 populations are shown in Fig. 9. Due to a large number of nodes in the 10 kV medium voltage DN and space limitations of this paper, the node voltages of the 750 V DC and 380 V low voltage AC are not shown in this section. The following only focuses on the node voltage display of the 10 kV DN. As shown in Fig. 9, the voltage distribution of each node is not uniform, and the node voltage under each population has exceeded the limit seriously. This is because the corresponding reactive power optimization measures have not been taken, and the reactive power resources in the DN have not been rationally used, resulting in poor node voltage quality and serious network loss. As shown in Fig. 10, the distribution of each population is roughly the same after volt/var control, indicating that the simulation results are convergent and reliable. After the preset number of iterations for reactive power optimization, the node voltages of DN under each population in Fig. 10 have been significantly improved compared with Fig. 9, and the situation of node voltage exceeding the limit rarely occurs, which shows that reactive power optimization is fully performed. The necessity of volt/var control and the effectiveness of the coordination measures between PET and photovoltaic converters is verified in this paper.

**Table 6**  
Case studies under different load levels.

Case studies		Load level		
		Light (50%)	Normal (100%)	Heavy (150%)
CLCM	Power loss (kW)	19.6643	39.4485	59.3726
	Voltage deviation (kV)	0.0878	1.0186	2.0687
Novel loss model	Power loss (kW)	13.5763	34.3186	62.4762
	Voltage deviation (kV)	0.0971	1.0104	2.0739

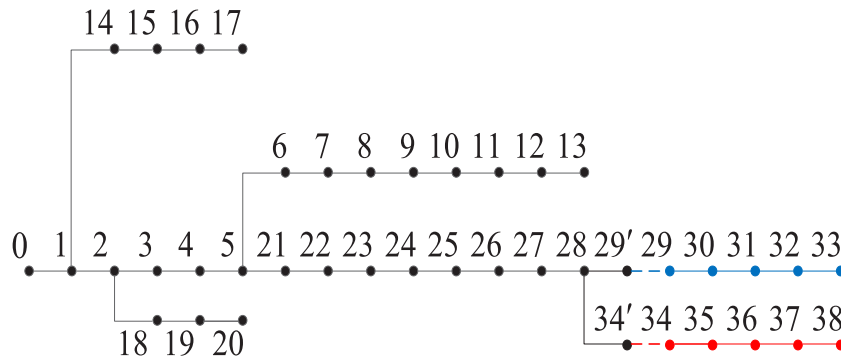


**Fig. 6.** Improved IEEE 33-bus system.

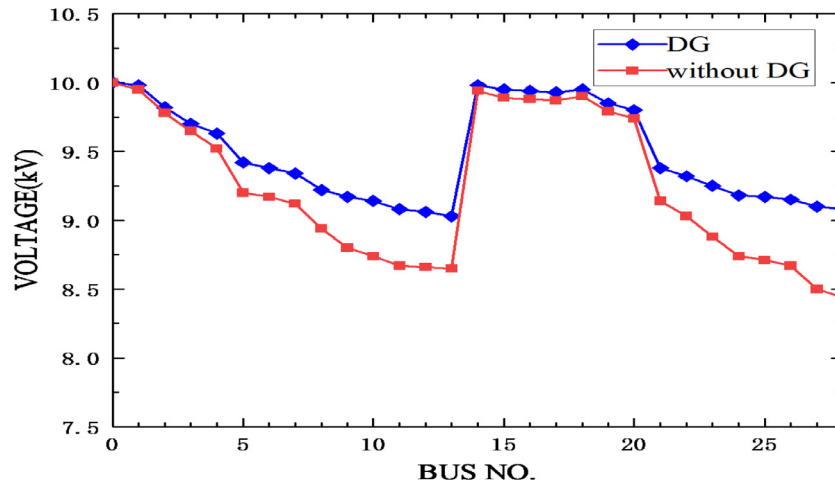


**Fig. 7.** High voltage AC system node voltage.

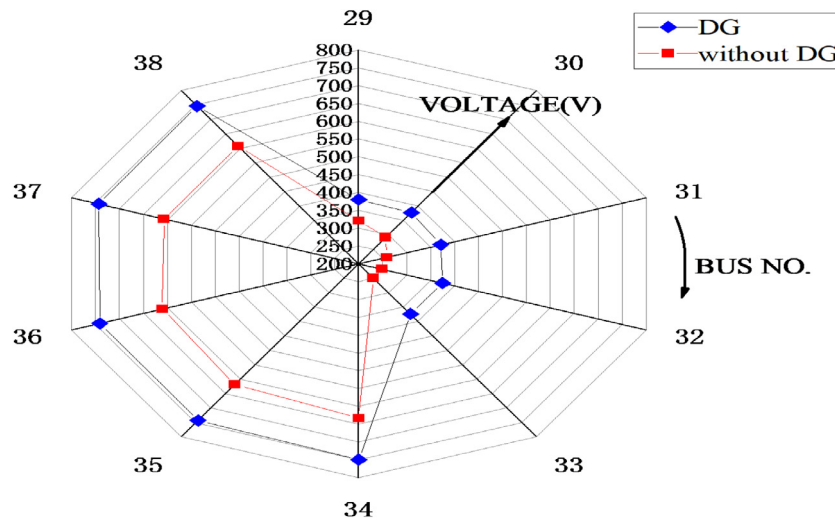


**Fig. 8.** Low voltage system node voltage.

**Table 7**  
The parameters of model.

Start node	End node	Impedance ( $\Omega$ )	Load of end node (kVA)
27	28	$0.5416 + j0.7129$	0
28	29'	$j3.21$	0
28	34'	$j3.21$	0
29	30	$0.0501 + j0.0080$	$60 + j20$
30	31	$0.0752 + j0.0120$	$60 + j20$
31	32	$0.0401 + j0.0064$	$60 + j20$
32	33	$0.0351 + j0.0056$	0
34	35	0.0165	150
35	36	0.0132	250
36	37	0.0149	150
37	38	0.0116	0

**Table 8**  
The parameters of DGs nodes.

Node	Active power (kW)	Reactive power (kvar)	Node type
28	120	80	PV
29	90	40	PV
33	90	40	PQ
34	80	0	P
38	250	0	P

**Table 9**  
Computational time under different load levels.

Load level	Iterations	Computational time (ms)	Convergence error
Light (50%)	10	36.8	$1.74 \times 10^{-14}$
Normal (100%)	7	35.6	$7.79 \times 10^{-14}$
Heavy (150%)	8	35.7	$1.95 \times 10^{-14}$

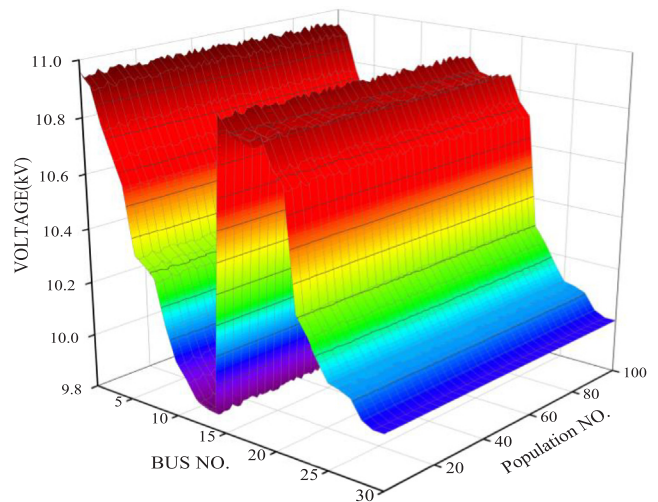


**Fig. 10.** Node voltage under 100 populations after optimization.

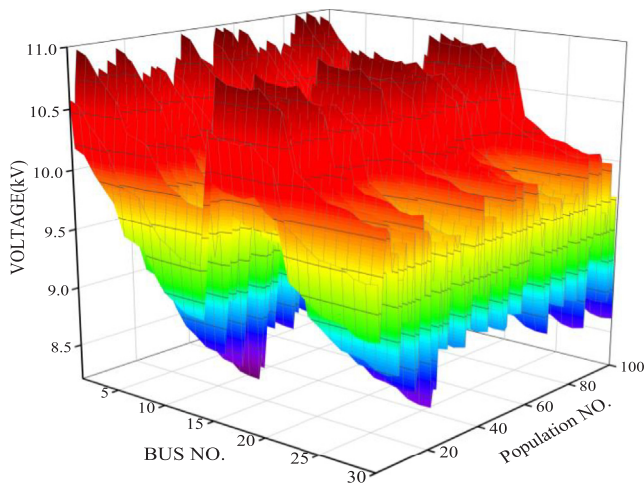


**Fig. 9.** Node voltage under initial 100 populations.

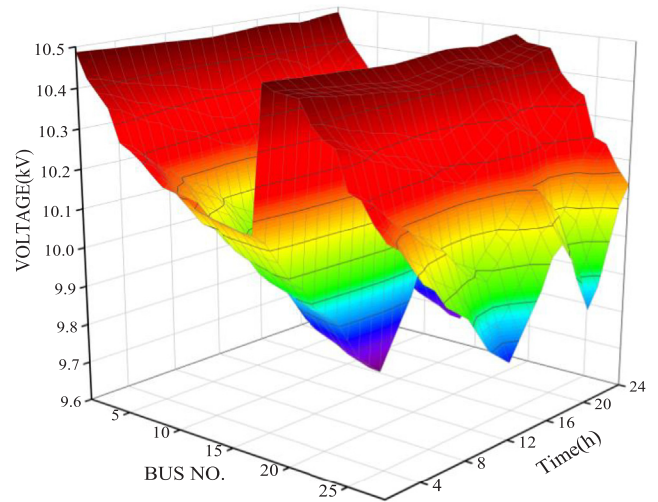


**Fig. 11.** Node voltage in different periods.

The above part of the simulation is based on the fixed load data. It is necessary to verify the reliability of the volt/var control in this paper under different load conditions. Monte Carlo simulation is used to generate 24 h AC–DC hybrid DN load data, and reactive power optimization control is adopted for the DN under different load conditions. The node voltage of the 10 kV DN at 24 h is presented in Fig. 11. Due to the evident random load fluctuations, the node voltage changes in different periods have certain differences, and it is impossible to achieve the same node voltages in all periods. The optimized node voltage in Fig. 11 has better quality, indicating that the reactive power control method in this paper can fully meet the demand of load fluctuations and has higher reliability.

The pareto solutions are presented in Fig. 12 and a solution is selected to acquire a trade-off result between  $f_1$  and  $f_2$ . The node

voltage obtained is shown in Fig. 13 and Fig. 14. It can be seen that the optimized node voltage has been significantly improved, especially for high-voltage ports. Through calculation, the objective function  $f_1$  is 39.49 kW before optimization and 34.10 kW after optimization. The total active power loss of DN after optimization is reduced by 13.6%. The proposed optimization model can not only improve the node voltage quality, but also reduce the active power loss of the system, which verifies the effectiveness of the optimization model.

## 6. Conclusion

As the penetration rate of DGs gradually increases, PET is widely used in AC–DC hybrid DN. The current research rarely considers the loss model of PET and its application in power flow calculation. This paper establishes an equivalent loss model of PET. The power flow calculation is carried out in the improved IEEE 33-bus system, and the results verify the feasibility of the power flow calculation including PET and distributed renewable generation. A multi-objective reactive power optimization model is proposed and solved by NSGA-II. The coordination between power loss and voltage deviation using PET and two types of PV converters simultaneously is implemented. The active power

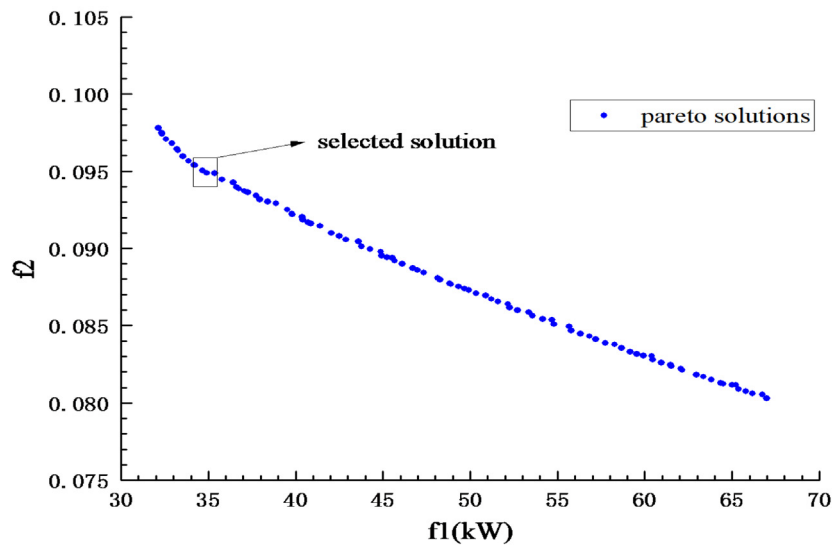


Fig. 12. Pareto solutions.

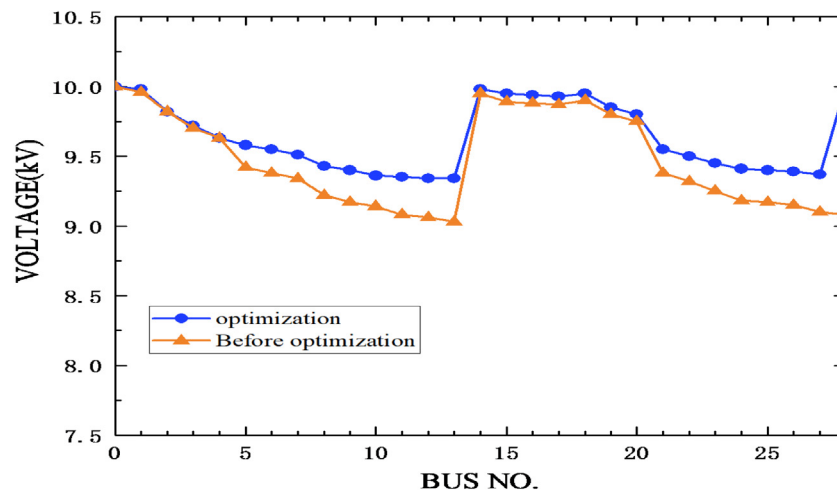


Fig. 13. High voltage AC system node voltage.

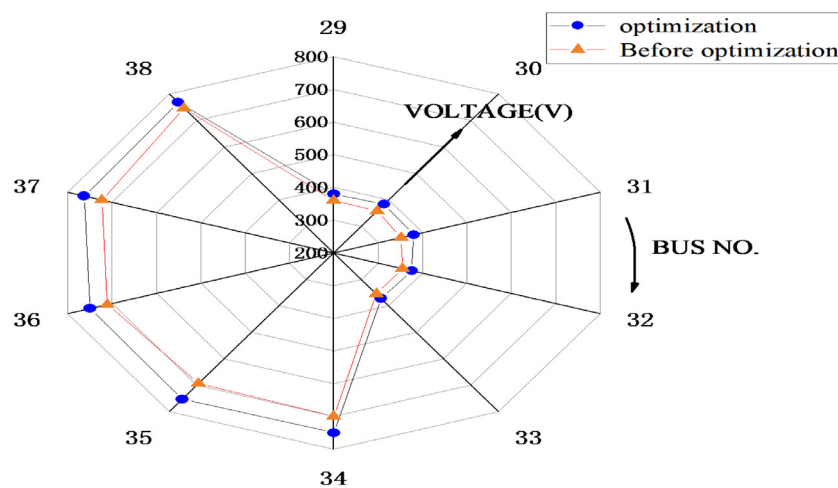


Fig. 14. Low voltage system node voltage.

loss of DN after optimization is reduced by 13.6%. The simulation results show that the optimized system node voltage is more reasonable, and the active power loss of the system is also reduced.

From the perspective of the power electronic devices, various measures can be studied to reduce the conduction and switching losses of power electronic devices and optimize the operation performance of PET. In addition, the time characteristics of the load and photovoltaic output, and the determination of optimal location and sizing for PET will be further investigated to combine with the multi-objective models proposed in this paper. The coordination between PET and other power electronic devices such as soft open points in DN can be further studied.

### CRedit authorship contribution statement

**Kun Yu:** Conceptualization, Investigation, Formal analysis, Methodology, Funding acquisition, Writing – original draft, Writing – review & editing. **Bu Xue:** Conceptualization, Methodology, Software, Writing. **Fangyuan Gu:** Data curation, Engine testing. **Haochen Hua:** Data curation, Grammar check. **Yubo Yuan:** Formal analysis, Investigation. **Qiang Li:** Data curation, Engine testing.

### Declaration of competing interest

The authors declare that they have no known competing financial interests or personal relationships that could have appeared to influence the work reported in this paper.

### Acknowledgments

This paper was supported by the National Natural Science Foundation of China (No. U1766203).

### References

- Ahmadi, H., Martí, J., Dommel, H., 2014. A framework for volt-VAR optimization in distribution systems. *IEEE Trans. Smart Grid* 6 (3), 1473–1483.
- Bahman, A., Ma, K., Blaabjerg, F., 2018. A lumped thermal model including thermal coupling and thermal boundary conditions for high-power IGBT modules. *IEEE Trans. Power Electron.* 33 (3), 2518–2530.
- Baliga, B., 2013. Analytical modeling of IGBTs: challenges and solutions. *IEEE Trans. Electron. Devices* 60 (2), 535–543.
- Bazzi, A., Krein, P., Kimball, J., et al., 2012. IGBT and diode loss estimation under hysteresis switching. *IEEE Trans. Power Electron.* 27 (3), 1044–1048.
- Bottura, R., Borghetti, A., 2014. Simulation of the volt/var control in distribution feeders by means of a networked multiagent system. *IEEE Trans. Ind. Inform.* 10 (4), 2340–2353.
- Christe, A., Dujic, D., 2017. Virtual submodule concept for fast semi-numerical modular multilevel converter loss estimation. *IEEE Trans. Ind. Electron.* 64 (7), 5286–5294.
- Coppo, M., Bignucolo, F., Turri, R., 2017. Generalised transformer modelling for power flow calculation in multi-phase unbalanced networks. *IET Gener. Transm. Distrib.* 11 (15), 3843–3852.
- Das, D., Hrishikesan, V., Kumar, C., et al., 2021. Smart transformer-enabled meshed hybrid distribution grid. *IEEE Trans. Ind. Electron.* 68 (1), 282–292.
- Flourentzou, N., Agelidis, V., Meijden, M., et al., 2010. Optimized modulation for AC-DC harmonic immunity in VSC HVDC transmission. *IEEE Trans. Power Deliv.* 25 (3), 1713–1720.
- Ghofrani, M., Majidi, M., 2021. A comprehensive optimization framework for EV-renewable DG coordination. *Electr. Power Syst. Res.* 194.
- Guerra, G., Martinez-Velasco, J., 2017. A solid state transformer model for power flow calculations. *Int. J. Electr. Power Energy Syst.* 89, 40–51.
- Haddadian, H., Noroozian, R., 2019. Multi-microgrid-based operation of active distribution networks considering demand response programs. *IEEE Trans. Sustain. Energy* 10 (4), 1804–1812.
- Hou, N., Li, Y., 2020. Overview and comparison of modulation and control strategies for a nonresonant single-phase dual-active-bridge DC-DC converter. *IEEE Trans. Power Electron.* 35 (3), 3148–3172.
- Howlader, A., Sadoyama, S., Roose, L., et al., 2018. Distributed voltage regulation using Volt-Var controls of a smart PV inverter in a smart grid: An experimental study. *Renew. Energy* 127, 145–157.
- Hua, H., Cao, J., Yang, G., et al., 2018. Voltage control for uncertain stochastic nonlinear system with application to energy internet: non-fragile robust H<sub>∞</sub> approach. *J. Math. Anal. Appl.* 463 (1), 93–110.
- Hua, H., Qin, Y., Hao, C., 2019. Optimal energy management strategies for energy internet via deep reinforcement learning approach. *Appl. Energy* 239, 598–609.
- Hua, H., Qin, Z., Qin, Y., et al., 2022. Data-driven dynamical control for bottom-up energy internet system. *IEEE Trans. Sustain. Energy* 13 (1), 315–327.
- Huang, L., Li, Y., Cui, Q., et al., 2020. Research on optimal configuration of AC/DC hybrid system integrated with multiport solid-state transformers and renewable energy based on a coordinate strategy. *Int. J. Electr. Power Energy Syst.* 119.
- Huber, J., Kolar, J., 2019. Applicability of solid-state transformers in today's and future distribution grids. *IEEE Trans. Smart Grid* 10 (1), 317–326.
- Ju, Y., Wu, W., Zhang, B., et al., 2014. An extension of FBS three-phase power flow for handling PV nodes in active distribution networks. *IEEE Trans. Smart Grid* 5 (4), 1547–1555.
- Kraiczy, M., Stetz, T., Braun, M., 2017. Parallel operation of transformers with on load tap changer and photovoltaic systems with reactive power control. *IEEE Trans. Smart Grid* 9 (6), 6419–6428.
- Liu, C., Li, X., Zhi, Y., 2018. New breed of solid-state transformer mainly combing hybrid cascaded multilevel converter with resonant DC-DC converters. *Appl. Energy* 210.
- Liu, L., Popov, M., Meijden, M., et al., 2017. Optimized control of LCL-VSC converter with refined s-parameter. *IEEE Trans. Power Deliv.* 32 (4), 2101–2110.
- Lu, F., Du, P., Liu, H., et al., 2019. Affine arithmetic-based power flow algorithm considering uncertainty for hybrid AC/DC grids incorporating VSCs. *IET Gener. Transm. Distrib.* 13 (10), 1856–1864.
- Ma, W., Wang, W., Chen, Z., et al., 2021. Voltage regulation methods for active distribution networks considering the reactive power optimization of substations. *Appl. Energy* 284.
- Madhusoodhanan, S., Tripathi, A., Patel, D., et al., 2020. Solid-state transformer and MV grid tie applications enabled by 15 kV SiC IGBTs and 10 kV SiC MOSFETs based multilevel converters. *IEEE Trans. Ind. Appl.* 51 (4), 3343–3360.
- Malekpour, A., Tabatabaei, S., Niknam, T., 2012. Probabilistic approach to multi-objective Volt/Var control of distribution system considering hybrid fuel cell and wind energy sources using improved shuffled frog leaping algorithm. *Renew. Energy* 39 (1), 228–240.
- Milczarek, A., Malinowski, M., 2020. Comparison of classical and smart transformers impact on MV distribution grid. *IEEE Trans. Power Deliv.* 35 (3), 1339–1347.
- Morshed, M., Fekih, A., 2020. A novel fault ride through scheme for hybrid wind/PV power generation systems. *IEEE Trans. Sustain. Energy* 11 (4), 2427–2436.
- Nazir, F., Pal, B., Jabr, R., 2018. A two-stage chance constrained volt/var control scheme for active distribution networks with nodal power uncertainties. *IEEE Trans. Power Syst.* 34 (1), 314–325.
- Parizad, A., Hatziaodoniou, K., 2020. Security/stability-based Pareto optimal solution for distribution networks planning implementing NSGAII/FDMT. *Energy* 192.
- Paul, S., Sharma, A., Padhy, N., 2021. Risk constrained energy efficient optimal operation of a converter governed AC/DC hybrid distribution network with distributed energy resources and Volt-VAR controlling devices. *IEEE Trans. Ind. Appl.* 57 (4), 4263–4277.
- Rohner, S., Bernet, S., Hiller, M., et al., 2010. Modulation, losses, and semiconductor requirements of modular multilevel converters. *IEEE Trans. Ind. Electron.* 57 (8), 2633–2642.
- Roshen, W., 2007. A practical, accurate and very general core loss model for nonsinusoidal waveforms. *IEEE Trans. Power Electron.* 22 (1), 30–40.
- Sadigh, A., Dargahi, V., Corzine, K., 2016. Investigation of conduction and switching power losses in modified stacked multicell converters. *IEEE Trans. Ind. Electron.* 63 (12), 7780–7791.
- Salles, D., Pinto, A., Freitas, W., 2016. Integrated volt/var control in modern distribution power systems based on support vector machines. *Int. Trans. Electr. Energy Syst.* 26 (10), 2216–2229.
- Shah, D., Crow, M., 2015. Online volt-var control for distribution systems with solid-state transformers. *IEEE Trans. Power Deliv.* 31 (1), 343–350.
- She, X., Huang, A., Burgos, R., 2013. Review of solid-state transformer technologies and their application in power distribution systems. *IEEE J. Emerg. Sel. Top Power Electron.* 1 (3), 186–198.
- Silva, E., Lima, A., Rossiter, M., 2020. Data-driven sensitivity coefficients estimation for cooperative control of PV inverters. *IEEE Trans. Power Deliv.* 35 (1), 278–287.
- Sun, X., Qiu, J., Zhao, J., 2021. Real-time volt/var control in active distribution networks with data-driven partition method. *IEEE Trans. Power Syst.* 36 (3), 2448–2461.
- Syed, I., Khadkikar, V., Zeineldin, H., 2018. Loss reduction in radial distribution networks using a solid-state transformer. *IEEE Trans. Ind. Appl.* 54 (5), 5474–5482.

- Taghavi, R., Seifi, A., Pourahmadi, M., 2012. Fuzzy reactive power optimization in hybrid power systems. *Int. J. Electr. Power Energy Syst.* 42 (1), 375–383.
- Tang, Z., Hill, D., Liu, T., 2021. Distributed coordinated reactive power control for voltage regulation in distribution networks. *IEEE Trans. Smart Grid* 12 (1), 312–323.
- Vijayan, V., Mohapatra, A., Singh, S.N., 2021. Demand response with Volt/Var optimization for unbalanced active distribution systems. *Appl. Energy* 300, 117361.
- Wang, H., Su, M., Sheng, K., 2017. Theoretical performance limit of the IGBT. *IEEE Trans. Electron. Devices* 64 (10), 4184–4192.
- Wang, Y., Zhang, Y., Wang, Y., et al., 2021. A dual-active-bridge with half-bridge submodules DC solid-state transformer for DC distribution networks. *IEEE J. Emerg. Sel. Top Power Electron.* 9 (2), 1891–1904.
- Xu, Y., Dong, Z., Zhang, R., et al., 2017. Multi-timescale coordinated voltage/var control of high renewable-penetrated distribution systems. *IEEE Trans. Power Syst.* 32 (6), 4398–4408.
- Xu, Y., Ho, C., Ghosh, A., et al., 2020. An electrical transient model of IGBT-diode switching cell for power semiconductor loss estimation in electromagnetic transient simulation. *IEEE Trans. Power Electron.* 35 (3), 2979–2989.
- Yeh, H., Gayme, D., Low, S., 2012. Adaptive VAR control for distribution circuits with photovoltaic generators. *IEEE Trans. Power Syst.* 27 (3), 1656–1663.
- Zhang, C., Xu, Y., 2020. Hierarchically-coordinated voltage/VAR control of distribution networks using PV inverters. *IEEE Trans. Smart Grid* 11 (4), 2942–2953.
- Zhu, Y., Xiao, M., Su, X., et al., 2020. Modeling of conduction and switching losses for IGBT and FWD based on SVPWM in automobile electric drives. *Appl. Sci. Basel* 10 (13).